Plastic anisotropy in pearlite

A molecular dynamics study with insights from the periodic bicrystal model

Liu, Kai; Shuang, Fei; Sluiter, Marcel H.F.

DOI
10.1016/j.actamat.2025.121100

Publication date
2025

Document Version
Final published version

Published in
Acta Materialia

Acta Materialia 294 (2025) 121100

Contents lists available at ScienceDirect

Acta Materialia

journal homepage: www.elsevier.com/locate/actamat

Full length article

Plastic anisotropy in pearlite: A molecular dynamics study with insights from the periodic bicrystal model

Kai Liu [a,*], Fei Shuang [a], Marcel H.F. Sluiter [a,b]

[a] Department of Materials Science and Engineering, Delft University of Technology, Mekelweg 2, Delft, 2628 CD, The Netherlands
[b] Department of Materials Science and Engineering, Faculty of Engineering, Ghent University (UGent), Technologiepark 903, Ghent, B-9052, Belgium

ARTICLE INFO

Keywords:
Pearlite
Cementite decomposition
Schmid factor
Bicrystal model
Molecular dynamics
Anisotropy

ABSTRACT

Cold-drawn pearlite wire is widely used in industry due to its exceptional high strength. Understanding the deformation mechanisms during the cold-drawing process of pearlite, particularly the deformation and decomposition of cementite, is of great significance. In this study, a bicrystal model tailored to lamellar structures is developed to calculate the elastic properties and stress concentration of pearlite. By analyzing slip activation in both ferrite and cementite, along with the yield strength, we reveal the significant influence of loading direction on pearlite deformability. Notably, the yield strength varies from 9.5 GPa to 17.0 GPa. Under specific loading conditions, plastic deformation is observed to initiate in cementite, challenging the conventional assumption that slip bands always originate in ferrite. Furthermore, factors that influence the plastic deformation of pearlite are discussed. A successive strengthening mechanism is proposed to explain the excellent deformability and high strength of pearlite after extensive deformation.

This work introduces a novel method for directional loading of lamellar structures. The surprising finding that plastic deformation, without fracture, can initiate in cementite, might offer directions for developing other structural materials with extreme tensile strength and deformability.

1. Introduction

Pearlite is a eutectoid steel microstructure with a lamellar morphology composed of ductile ferrite (α-phase) and brittle cementite (θ-phase). For pearlite obtained from the eutectoid transformation, the volume ratio of the two phases, V_α/V_θ, is approximately 8. After heavy cold-drawing deformation, pearlite can reach strengths up to 7 GPa, approaching the theoretical strength of steel [1]. During the cold drawing process, the inter-lamellar spacing decreases [2], dislocation density increases, and cementite lamellae gradually decompose. Supersaturated carbon atoms released from cementite dissolve into the ferrite lattice, causing significant lattice distortion [3]. This synergistic combination of dislocation strengthening, solid solution strengthening, and grain refinement is regarded as the primary mechanism behind the ultrahigh strength of pearlite [4,5]. Understanding the structural evolution of pearlite and the critical role of cementite decomposition during drawing is crucial for optimizing its engineering performance.

Bulk cementite is generally considered a brittle ceramic with low fracture toughness [6,7]. Its plastic deformation has been observed in limited scenarios, such as nano-indentation [8], compression [9], and multi-pass sliding wear [10]. The dislocation patterns in cementite were characterized in several early studies [11,12]. The plasticity of cementite is sensitive to temperature [9,11]. Terashima et al. showed that under compression, 2% plastic deformation was achievable at 573 K, while brittle fracture dominated at room temperature [9].

In pearlite, where cementite is embedded in ferrite, its deformation behavior becomes more complex. Zhang et al. [2] observed cementite lamellae rotating, thinning, and fracturing during drawing of pearlite. The slip bands in cementite were found to be parallel to ferrite slip planes, suggesting slip initiation in ferrite followed by transfer to cementite. Zhou et al. [13] reported a transition in cementite from single crystalline to nanocrystalline and, eventually, to an amorphous state during pearlite deformation. Atom probe tomography has provided quantitative measurements of carbon concentrations in pearlite before and after deformation [14,15], revealing that the main mechanisms for cementite decomposition are dislocation-assisted carbon diffusion [15] and carbon segregation at sub-grain boundaries in ferrite [14].

To observe the dynamic deformation process, synchrotron diffraction has been used to study stress-partitioning between ferrite and cementite [16,17]. Digital image correlation revealed significant strain heterogeneity in pearlite, with strain concentration in specific colonies [10,18,19]. Tanaka et al. [20] identified room-temperature plastic deformation in cementite lamellae aligned parallel to the tensile direction.

* Corresponding author.
E-mail address: kailiou2035@gmail.com (K. Liu).

https://doi.org/10.1016/j.actamat.2025.121100
Received 11 February 2025; Received in revised form 25 April 2025; Accepted 1 May 2025
Available online 21 May 2025

Experimental studies of cementite deformation are challenging due to the small scales and large deformations involved. Molecular dynamics (MD) simulations provide a powerful complementary approach to probe the dynamic features of slip behavior in ferrite and cementite, offering insights into the deformation mechanisms of pearlite. Since interatomic potentials with special attention on cementite mechanical properties were developed [21,22] and the interfacial structures between ferrite and cementite with several orientation relations (ORs) have been systematically explored [23], MD simulations are expected to qualitatively correspond to the deformation process of pearlite. Guziewski et al. [24] investigated the effects of supercell size, volume fraction, and loading direction on pearlite yield strength and flow stress using a bicrystal model. Their study revealed that dislocation loops initiate at the α-θ interface. In a subsequent study, the plastic deformation and yield strength of pearlite under various ORs were systematically explored [25]. The slip activities in cementite were attributed to slip transmission from ferrite and the geometric relationships between slip systems in the two phases and loading directions were highlighted. Yu et al. [26] studied the tensile behavior of inclined pearlite lamellae and reported structural transformations in ferrite and cleavage cracks in cementite near the interface. Shimokawa et al. [27] found that interfacial dislocations significantly influence the pearlite deformation mechanisms. Using knowledge of the stress field induced by interfacial dislocations and applying Schmid factor analysis, they examined slip activation at the interface. In addition, MD simulations have been used to investigate fatigue [28] and nano-indentation deformation [29] in pearlite.

MD simulations of pearlite are often complemented by analytical models to calculate stress and strain states in each phase. For example, Guziewski et al. [24,25] used composite theory, based on iso-strain or iso-stress assumption, to estimate the elastic properties of pearlite. Shimokawa et al. [27] considered the strain compatibility at the interface using directional Poisson ratios for the two phases. However, these methods [24,25,27] have two major drawbacks. First, the elastic tensors for the two phases are simplified into Young's moduli and Poisson ratios, which is insufficient for the consideration of the interface compatibility. It can be inferred from the near-full elastic tensor of pearlite [30]. Second, the iso-strain and iso-stress assumptions are established based on specific loading directions and are not generally applicable.

Initially, an analytical approach to calculate stress partitioning between phases was developed [31] and then further applied to periodic twin boundaries [32]. In this study, a similar analytical model is applied to investigate the stress and strain states in pearlite under complex loading conditions (Section 2). For the Bagaryatskii OR, the analysis highlights the critical influence of loading direction on the magnitude of nominal Schmid factors for slip systems in both cementite and ferrite.

Previous MD studies on the deformation of pearlite have been limited to a few specific orientations, and therefore do not sufficiently capture the general deformation behavior of pearlite. By defining non-orthogonal supercells, we explored the deformation process of pearlite under multiple loading directions for the first time, as detailed in Section 3. Simulation results, including the yield strength, slip behaviors in ferrite and cementite, and the corresponding nominal Schmid factors for active slip systems, are presented in Section 4. Finally, in Section 5, we discuss the key factors influencing the plasticity of pearlite and provide insights into its deformation mechanisms.

2. Analytical model for pearlite mechanical properties

2.1. Bicrystal model for periodic composite

As the elastic properties of ferrite (α) and cementite(θ) differ, the two phases respond distinctly when pearlite is subjected to loading. To maintain deformation compatibility, an additional stress field arises at the interface, known as the incompatibility stress [33]. The bicrystal model representing pearlite is shown in Fig. 1. The volume fractions of cementite and ferrite are V_θ and V_α, respectively. The interface plane is set parallel to the XOZ plane. The following constraints apply to the model [34].

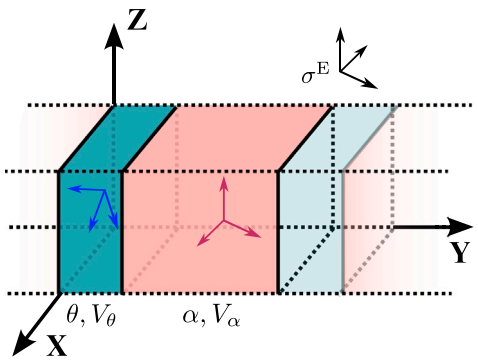

Fig. 1. Schematic representation of the bicrystal model for pearlite with a layered periodic structure. Ferrite (α) and cementite (θ) layers are infinitely extended in the XOZ plane, with volume fraction of V_α and V_θ. The interface is perpendicular to the Y-axis. The external stress σ^{E} can be of any type. For the Bagaryatskii OR, the crystallographic orientations of the two phases are given in Table 2.

(i) The two phases are rigidly glued to each other. No relative motion is allowed at the interface.
(ii) All the interfaces are parallel and infinitely extended in the XOZ plane.
(iii) For each phase, there is a linear relation between stress and strain.

With Voigt notation (xx → 1, yy → 2, zz → 3, yz → 4, xz → 5, xy → 6) with the engineering convention ($\varepsilon_4 = 2\varepsilon_{xy}$), the constitutive equation of linear elastic material is

$$\begin{bmatrix} \varepsilon_1 \\ \varepsilon_2 \\ \varepsilon_3 \\ \varepsilon_4 \\ \varepsilon_5 \\ \varepsilon_6 \end{bmatrix} = \begin{bmatrix} s_{11} & s_{12} & s_{13} & s_{14} & s_{15} & s_{16} \\ s_{12} & s_{22} & s_{23} & s_{24} & s_{25} & s_{26} \\ s_{13} & s_{23} & s_{33} & s_{34} & s_{35} & s_{36} \\ s_{14} & s_{24} & s_{34} & s_{44} & s_{45} & s_{46} \\ s_{15} & s_{25} & s_{35} & s_{45} & s_{55} & s_{56} \\ s_{16} & s_{26} & s_{36} & s_{46} & s_{56} & s_{66} \end{bmatrix} \begin{bmatrix} \sigma_1 \\ \sigma_2 \\ \sigma_3 \\ \sigma_4 \\ \sigma_5 \\ \sigma_6 \end{bmatrix} \tag{1}$$

According to the first constraint listed above, strain components inside the interface plane should be continuous,

$$\varepsilon_i^\theta - \varepsilon_i^\alpha = 0, \quad i,j = 1,3,5. \tag{2}$$

The tractions on the GB must be continuous, and the difference at the GB must vanish,

$$\sigma_i^\theta - \sigma_i^\alpha = 0, \quad i = 2,4,6. \tag{3}$$

When under an arbitrary far-field external stress σ^{E}, global stress equilibrium requires

$$\frac{1}{V}\int_V \sigma_i dV = \sigma_i^{\mathrm{E}}, \tag{4}$$

where σ^{E} is the applied external stress [31]. For pearlite,

$$\sigma_i^{\mathrm{E}} = V^\theta \sigma_i^\theta + V^\alpha \sigma_i^\alpha. \tag{5}$$

For arbitrary ORs and volume fractions of the two phases, the above equations holds. In this study the Bagaryatskii OR [35] is adopted, as $[010]_\theta \| [111]_\alpha$, $[100]_\theta \| [1\bar{1}0]_\alpha$, and $(001)_\theta \| (\bar{1}\bar{1}2)_\alpha$.

The modified embedded atom method (MEAM) potential for Fe-C system developed by Liyanage et al. [22] was applied because it gives a good representation of both ferrite and cementite. Additionally, it has been used widely for simulating pearlite deformation [23,36,37]. The elastic tensor components for the two phases are shown in Table 1.

Table 1
Elastic tensor components for ferrite and cementite (with $a < b < c$) at 0 K, except where noted otherwise. In DFT calculations two GGA implementations were used: PW91 [39] and PBE [40]. For cementite calculations are listed that include internal relaxations. Such relaxations are essential for accurate results [41].

	Modulus (GPa)	C_{11}	C_{22}	C_{33}	C_{23}	C_{13}	C_{12}	C_{44}	C_{55}	C_{66}
Ferrite	MEAM [22]		213			143			119	
	Experiment [42]		243			138			122	
	Experiment [43]		240			136			121	
	PW91[a] [44]		277			147			96	
Cementite	MEAM [22]	326	303	249	135	119	163	72	27	98
	PBE[b] [45]	316	385	341	157	167	162	131	13	131
	PBE[a] [38]	322	388	345	156	162	164	134	15	134
	PBE[b] [38]	325	395	347	158	163	169	135	18	134
	PBE[b] [46]	319	393	340	144	149	141	114	−60	145
	PBE[b] [47]	323	388	344	155	160	145	135	18	132
	PW91[b] [48]	298	375	339	161	172	144	30	13	132
	PBE[b] [49]	300	383	344	162	162	156	135	28	134
	PBE[c] [49]	299	315	321	136	175	131	138	24	142
	PBE[d] [49]	309	354	340	146	171	137	131	33	129

[a] Energy-strain method.
[b] Stress–strain method.
[c] Including quantum-harmonic corrections at 0 K.
[d] Including quantum-harmonic corrections at 400 K.

For cementite the MEAM potential aims to reproduce the elastic tensor values of Jiang et al. [38], but as Table 1 shows, the MEAM values are representative for a wide spectrum of DFT results.

The compliance matrix S was determined through the strain response of the pearlite bicrystal model under the six independent unit stress states (σ_1 to σ_6). The stiffness matrix C is obtained by inverting S.

2.2. Orientation-dependence of nominal Schmid factors

The Schmid factor m quantifies the effectiveness of a loading direction for activating a specific slip system. In its classical formulation, m is defined on purely geometric considerations in a homogeneous material under uniaxial stress conditions: $m = \cos\phi\cos\lambda$, where ϕ is the angle between the slip plane normal and the loading direction, and λ is the angle between the slip direction and the loading direction. This definition inherently limits m to values ≤ 0.5, with the maximum achieved when $\phi = \lambda = 45°$. However, this formulation becomes inapplicable for describing slip system activation in non-homogeneous materials, and under non-uniaxial stress states, which are common in heterogeneous materials.

In pearlite, the presence of α-θ interfaces introduces significant incompatibility, as revealed by the bicrystal model. Even under macroscopic uniaxial loading of pearlite, the local stress states σ^{local} in α and θ deviate from uniaxial. To properly characterize slip system activation in these complex stress states, we introduce the nominal Schmid factor m_{n}, defined as:

$$m_{\text{n}} = \frac{\tau^{\text{local}}}{\sigma^{\text{uniaxial}}}, \tag{6}$$

where the local resolved shear stress τ^{local} is calculated through the full stress tensor formulation:

$$\tau^{\text{local}} = \boldsymbol{\sigma}^{\text{local}} : (\mathbf{m} \otimes \mathbf{n}), \tag{7}$$

with $\boldsymbol{\sigma}^{\text{local}}$ being the local stress tensor, and $\mathbf{m}$ and $\mathbf{n}$ are unit vectors describing the slip direction and the normal to the slip plane, respectively [50]. This stress-based formulation is mathematically equivalent to the normalized resolved shear stress approach employed by Tiba et al. [51] in their study of nickel bicrystals (see Table 3), where grain boundary incompatibility stresses were similarly incorporated. The key advantage of m_{n} is its ability to account for both the local stress concentration effects and the crystallographic orientation of slip systems. Similar extensions of the Schmid factor have been proposed in the literature to address complex stress states [52,53].

For ferrite, 24 $\{110\}\langle 111\rangle$ and $\{112\}\langle 111\rangle$ slip systems are considered. For cementite, all slip systems suggested by experiments are considered [8,10,12]: (100)[001], (100)[010], (010)[001], (010)[100], (001)[010], (001)[100], and (001)[110].

For a given σ^{uniaxial} along a certain direction, the highest m_{n} among all available slip systems indicates the maximum resolved shear stress for possible slip activity. Fig. 2 illustrates the highest m_{n} for slip systems in α (a) and θ (b) under uniaxial stress applied along various directions. The loading directions are projected on the XOZ stereographic plane. The volume ratio between ferrite and cementite is set as $V_\alpha/V_\theta = 8$.

For α, which exhibits high crystallographic symmetry and multiple slip systems, the highest m_{n} ranges from 0.32 to 0.502. In contrast, the θ phase, due to its lower symmetry and fewer slip systems, shows a much wider range of the highest m_{n} values (0 to 1.02), with strong orientation dependence. Notably, the maximum values of highest m_{n} among all loading directions for both phases exceed the traditional Schmid factor limit of 0.5. The observed increase of m_{n} originates from two factors:

(i) Definition: while m depends solely on the geometric factor ($\cos\phi\cos\lambda$) under uniaxial stress, m_{n} incorporates the complete local stress state as $\tau^{\text{local}}/\sigma^{\text{uniaxial}}$. The stress-based formulation naturally accounts for stress concentration effects. As a result, m_{n} is not constrained by the geometric limit of 0.5 and can exceed 1 in regions of significant stress concentration. E.g. when applying uniaxial loading to long, parallel fibers, the least compliant fibers will carry most of the load.

(ii) Strong incompatibility stress. The exceptionally high resolved shear stress for slip systems in θ originates from the incompatibility stress at the α-θ interface. Previous studies on nickel bicrystals under uniaxial compression reported m_{n} values up to 0.63 (Table 3 [51]), attributed to incompatibility stresses at the grain boundary. In pearlite, the larger volume fraction difference ($V_\alpha/V_\theta = 8$), and the stronger elastic contrast between α and θ compared to the nickel bicrystal amplify the incompatibility stress, especially in θ. The concentration of the incompatibility stress in the minority phase increases m_{n} values up to 1.02. Furthermore, in [51], the experimentally observed slip system activations agreed well with the calculated m_{n}. This indicates that m_{n} is a proper metric for slip activation in heterogeneous materials.

Fig. 2 also illustrates the loading directions used in the MD study of the mechanical behavior of pearlite. Previous MD simulations involving the plasticity of pearlite [24,26–28,54] focused on loading directions with low m_{n} in cementite, as indicated by the diamond symbols in the

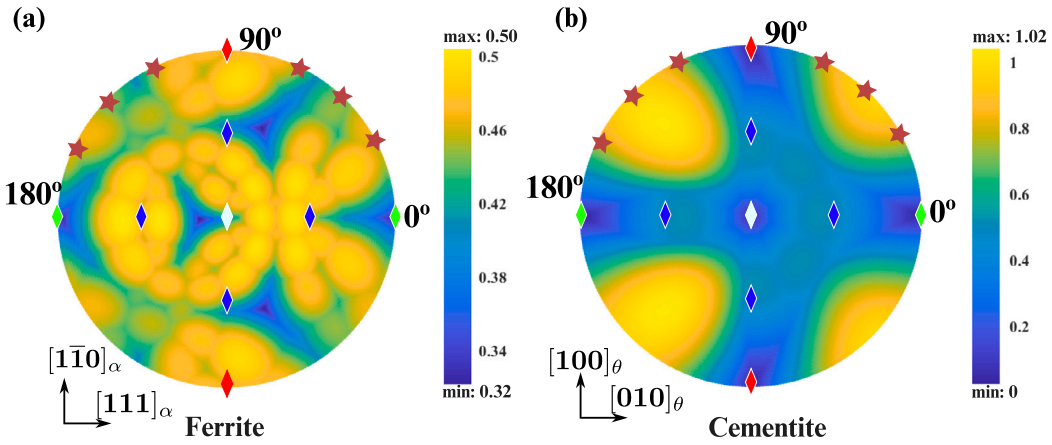

Fig. 2. Highest nominal Schmid factors m_n in (a) ferrite and (b) cementite for a pearlite structure under uniaxial stress applied along various directions. The loading directions are represented on the XOZ stereographic projection. The value of the highest m_n varies from 0.32 to 0.50 for ferrite and 0 to 1.02 for cementite. Diamond markers indicate the specific directions studied in previous MD simulations: green [24,25,54,57], red [24,25,27,28,54,57], blue [26], white [24,25,37]. This study focuses on loading within the XOZ plane, highlighted by the brown stars, green diamonds and red diamonds, corresponding to loading in the $(11\bar{2})_\alpha$ and $(001)_\theta$ planes. (For interpretation of the references to color in this figure legend, the reader is referred to the web version of this article.)

stereographic projection. In this work, we focus on loading directions marked by the brown stars. The choice of these directions is based on two considerations:

(i) The range of m_n in cementite for these directions is between 0 and 0.95, providing a representative overview of the deformation behavior of pearlite.
(ii) Experimental observations indicate that during processes such as rolling or drawing, pearlite tends to align with the loading direction [55,56]. As a result, loading in the interface plane (here the XOZ plane) closely approximates the actual loading conditions in these scenarios.

To compare with previous work, loading directions marked by blue and red diamonds are included in this study also.

2.3. Influence of the volume ratio

As shown explicitly in Eq. (5), the volume fraction of the two phases significantly influences the partitioning of incompatibility stress across the interface. Here we use the ratio between hydrostatic stress $\sigma^h = (\sigma_1+\sigma_2+\sigma_3)/3$ and the external stress $\sigma^E = \sigma_2$ ($\sigma_i = 0 \ \forall \ i = 1,3-6$) to show the magnitude of stress concentration. Fig. 3(a) illustrates the effect of V^α/V^θ on σ^h/σ^E in the two phases. Without incompatibility stress at the interface, $\sigma^h/\sigma^E = 1/3$, corresponding to the horizontal dashed gray line. The magnitude of the additional stress field in each phase is inversely proportional to its volume fraction, which means phases with small volume fractions bear high additional stresses. For pearlite with $V^\alpha/V^\theta = 8$, σ^h/σ^E in cementite approaches 0.52, showing a 57% increase over the value without incompatibility stress. Fig. 3(b) and (c) depict the highest m_n for each loading direction in α and θ, respectively. The loading direction corresponds to the arc shown in Fig. 2(b), with the angle measured relative to the X-axis. All slip systems listed in the previous section are considered. For both phases, a decrease in V^θ/V^α leads generally to an increase in the m_n. Supercells with V^θ/V^α of 4 and 8 show rather similar stress levels and m_n. Therefore in the MD simulations we adopt supercells with $V^\theta/V^\alpha = 4$ to conserve computational resources.

3. Molecular dynamics simulation of pearlite

With the MEAM potential, the lattice parameter for BCC iron is $a^\alpha = 2.851$ Å. For Fe_3C, using the convention $a < b < c$, $a^\theta = 4.470$ Å, $b^\theta = 5.088$ Å, and $c^\theta = 6.670$ Å. To model pearlite using the Bagaryatskii OR with a periodic supercell, the supercell needs to be periodic for both α and θ simultaneously. Labeling the edges of the supercell as XYZ, the XOZ plane is chosen parallel with the α-θ interface which is coherent with the analytical model introduced in Section 2.

To create a pearlite supercell with minimum strain for both α and θ, the supercell edge length along X and Z needs to be an integer times a periodic vector for each of the two phases. Supercell dimensions that make for a near perfect match between both phases are shown in Table 2. The mismatch strain ε_i^m is estimated as

$$\varepsilon_i^m = 2(L_i^\theta - L_i^\alpha)/(L_i^\theta + L_i^\alpha), \tag{8}$$

where $i = X, Z$. Note that the mismatch strain is a different concept than the misfit strain. Using the elastic constants, the stresses induced by the mismatch strain in both phases are estimated to be less than 0.5 GPa, which is significantly smaller than the yield strength presented later.

Initiation of plastic deformation occurs independently in pearlite layers. Periodic boundary conditions may cause unrealistic results during MD simulations through artificial images when slip in one layer affects the slip behavior in other layers. Here we employ a pearlite supercell with two α-θ layers and four interfaces, as shown in Fig. 4(a) to reduce such artifacts.

During MD simulations, uniaxial loading is performed most conveniently along directions corresponding to supercell edges or perpendicular to supercell faces. Thus, to investigate the effect of loading direction on plastic deformation in pearlite, equivalent supercells with various edges were constructed, see Fig. 4(b), with distinct orientations along the longer edge in the XOZ plane, see Fig. 4(c). The cell lengths of the original cubic cell are $L_X = 163.03$ Å and $L_Z = 80.64$ Å. The angles between loading direction and $[010]_\theta \| [111]_\alpha$ were calculated as

$$\phi = tan^{-1}\frac{i \cdot L_Z}{L_X} \tag{9}$$

for loading along the slanted supercell edge and for loading perpendicular to the slanted supercell edge as

$$\phi = 90° + tan^{-1}\frac{i \cdot L_Z}{L_X}, \tag{10}$$

where $i = -1, 0, 1, 2$. This gives angles of 0°, 26°, 45°, 64°, 90°, 116°, 135°, 154° (rounded) in the various equivalent supercells. In the following sections, these angles are used to denote uniaxial tensile straining simulations along the corresponding directions.

Considering the symmetry of the pearlite in directions perpendicular to its stacking direction, ferrite exhibits mirror symmetry with respect

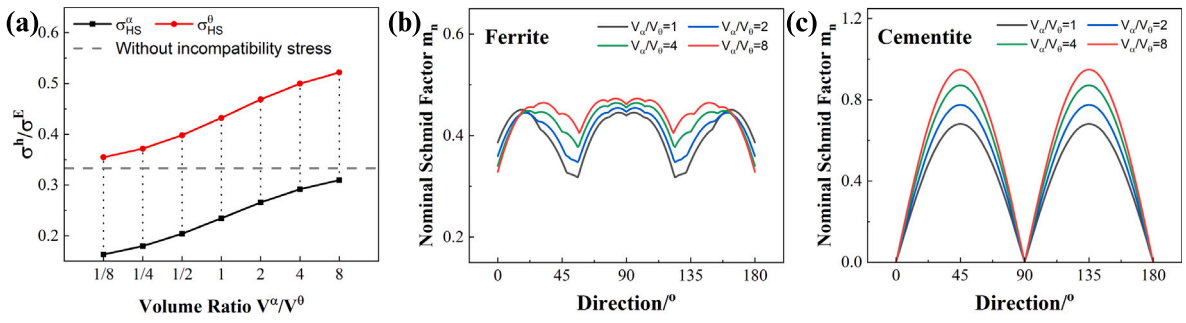

Fig. 3. Influence of the volume ratio of ferrite and cementite on the stress partition in the two phase. (a) Hydrostatic stress in α and θ under unit σ_1^E. Hydrostatic stress for a unit normal stress is 1/3, as shown with the dashed gray line. (b) and (c) show the highest nominal Schmid factor m_n for each loading direction within the XOZ plane in ferrite and cementite, respectively. The angle for the loading direction is with respect to X-axis, shown in Fig. 2(b). All slip systems listed in the previous section are considered.

Table 2
The dimensions of the pearlite supercell in the Bagaryatskii crystal orientation and the mismatch strains on the interface, using MEAM interatomic potential by Liyanage et al. [22].

Phase	item	X $[010]_\theta \| [111]_\alpha$	Y $[001]_\theta \| [\bar{1}\bar{1}2]_\alpha$	Z $[100]_\theta \| [1\bar{1}0]_\alpha$
Cementite	Unit cell(Å)	$b^\theta = 5.088$	$c^\theta = 6.670$	$a^\theta = 4.470$
	Supercell	$L_X^\theta = 32 \times 5.088 = 162.816$	$L_Y^\theta = 7.6 \times 6.670 = 50.692$	$L_Z^\theta = 18 \times 4.470 = 80.46$
Ferrite	unit cell(Å)	$a^\alpha \times \frac{\sqrt{3}}{2} = 2.469$	$a^\alpha \times \sqrt{6} = 6.983$	$a^\alpha \times \sqrt{3} = 4.032$
	Supercell	$L_X^\alpha = 66 \times 2.469 = 162.954$	$L_Y^\alpha = 30 \times 6.983 = 209.490$	$L_Z^\alpha = 20 \times 4.032 = 80.640$
Pearlite	Mismatch strain,Eq. (8)	−0.08%	N/A	−0.22%
	Relaxed Supercell(Å)	$L_X = 163.03$	$L_Y = 515.73$	$L_Z = 80.64$

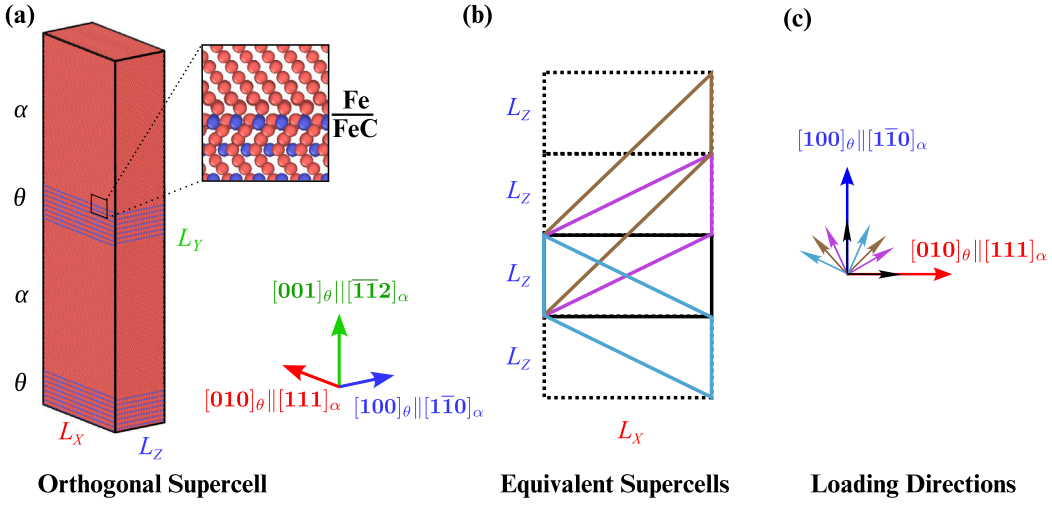

Fig. 4. (a) Two-layer pearlite supercell with Bagaryatskii OR used for MD simulations. In the original supercell, X (Z) corresponds to $[010]_\theta \| [111]_\alpha$ ($|[100]_\theta \| [1\bar{1}0]_\alpha$). The $\alpha - \theta$ interface is FeC-Fe which was reported to have the lowest interfacial energy [24]. FeC-Fe means that at the cementite side the nearest layer at the interface is FeC and next nearest layer is Fe. Equivalent supercells are defined by replacing the horizontal supercell edge with the slanted vectors (in color), as shown in (b). (c) displays the loading directions within the XOZ plane, both along and perpendicular to the slanted supercell edges. Directions are colored according to the corresponding equivalent supercells shown in (b). The red arrow corresponds to the 0° loading angle. (For interpretation of the references to color in this figure legend, the reader is referred to the web version of this article.)

to the $(1\bar{1}0)_\alpha$, while cementite features a $(001)_\theta$ mirror plane and a $(100)_\theta$ glide plane. When considering elasticity in continuum mechanics, a mirror symmetry appears with $(100)_\theta$ because cementite has an orthorhombic lattice. Therefore Bagaryatskii pearlite in our supercell exhibits mirror symmetry about the XOY plane in continuum elasticity. When discussing the atomic-scale structure of interfaces, this mirror symmetry does not exist.

The α-θ interface structure for the Bagaryatskii OR was systematically examined by Guziewski et al. [24]. The FeC-Fe interface, see Fig. 4(a), which means the interfacial chemistry is FeC on the side of cementite, was found to be energetically favorable. Here, we implemented this interface structure by selectively removing several atom layers in the cementite, resulting in a non-integer unit cell replication count in cementite along the stacking direction, as shown in Table 2.

Following relaxation at 300 K for 20 ps with a Nose–Hoover thermostat, uniaxial strain was applied along one side of the supercell, as depicted in Fig. 4(c). During tensile testing, normal stresses in directions orthogonal to the applied strain were maintained at zero and the temperature was kept at 300 K. A strain rate of $1 \times 10^9 s^{-1}$ was employed, consistent with previous studies [27,58]. For each load direction, three independent simulations were performed with different random initial velocities to ensure consistency.

It should be noted that shear strains are constrained to zero during tensile simulations for the following reasons:

Table 3
Stress and strain components applied on supercells induced by $\sigma_1 = 1$ GPa loading along various directions. The stress and strain components are given in the local coordinate system, where σ_1 is along the (local) loading direction and the local y-axis is aligned with the global Y-axis.

	0°	26°	45°	64°	90°	116°	135°	154°
σ_4 (GPa)	0	0.09	0.06	−0.10	−0.19	−0.10	0.06	0.09
σ_5 (GPa)	0	−0.14	−0.03	0.10	0	−0.10	0.03	0.14
σ_6 (GPa)	0	0.05	0.18	0.17	0	−0.17	−0.18	−0.05
$\varepsilon_1 \times 10^3$	3.7	4.5	5.5	4.9	4.2	4.9	5.5	4.5
$\varepsilon_2 \times 10^3$	−0.9	−1.0	−1.2	−1.4	−1.5	−1.4	−1.2	−1.0
$\varepsilon_3 \times 10^3$	−0.9	−1.7	−2.4	−1.7	−0.9	−1.7	−2.4	−1.7

(i) Due to the low symmetry of pearlite, the simulation box under uniaxial stress naturally develops shear strain. This complicates the determination of slip plane indices and resolved shear stresses and obfuscates analysis.
(ii) Previous MD studies on pearlite employed orthogonal simulation boxes, thereby eliminating shear strains. Adopting the same constraint allows for comparison with previous studies.

For each tensile direction (direction "x"), we constrain the three shear strains to zero and set the normal stresses in the two directions perpendicular to the loading direction to zero. With Voigt notation (loading direction "x", stacking direction "y"), the stress and strain components for current loading condition are calculated:

$$\sigma = C^p \cdot \varepsilon, \tag{11}$$

where $\sigma = [\sigma_1, 0, 0, \sigma_4, \sigma_5, \sigma_6]$, $\varepsilon = [\varepsilon_1, \varepsilon_2, \varepsilon_3, 0, 0, 0]$, and C^p is the elastic matrix for pearlite (as described in Section 2). For $V^\theta/V^\alpha = 4$, using the elastic tensor components for ferrite and cementite shown in Table 1(MEAM), the pearlite elastic tensor (in GPa) under 0° loading direction is given as,

$$C^p = \begin{bmatrix} 319 & 98 & 102 & 0 & 0 & -1 \\ & 283 & 119 & 0 & 0 & -31 \\ & & 299 & 0 & 0 & 33 \\ & & & 62 & 21 & 0 \\ & symmetric & & & 64 & 0 \\ & & & & & 64 \end{bmatrix}. \tag{12}$$

For other loading directions C^p must be rotated. It should be remarked that the pearlite supercell has an orthorhombic shape, but not orthorhombic symmetry due to the absence of mirror planes perpendicular to X and Y. For $\sigma_1 = 1$ GPa along various directions, the resulting stress and strain components of the supercells are listed in Table 3. The stress components are expressed in a local Cartesian coordinate system, where σ_1 aligns with the loading direction and the local y-axis is aligned with the global Y-axis. In particular, the shear stress can reach 19% of the tensile stress in the loading direction. In previous MD studies on pearlite, the additional shear stresses arising from the low symmetry of pearlite are overlooked [24,25,28,54]. This oversight leads to an incomplete understanding of the stress state and its influence on the deformation mechanisms.

The unit cell model for cementite was obtained from the Materials Project database (mp-510623) [59]. The construction of the supercell was carried out using Atomsk [60]. MD simulations were performed with the Large-scale Atomic/Molecular Massively Parallel Simulator (LAMMPS) [61], and the results were analyzed and visualized using OVITO 3.7.4 [62].

4. Results

4.1. Tensile behavior for pearlite

Fig. 5 presents the stress–strain curves for tensile deformation along eight different loading directions. For all directions, the initial response is nearly linear, with stress increasing proportionally with strain. Both the tensile modulus and maximum stress exhibit significant variation across these loading directions. As in prior work [25,27] we identify the maximum stress as the yield point. After yielding, the stress quickly drops to around 5 GPa and stabilizes at this level, except in 135° supercell, where stress decreases to a negative value post-yield. Utilizing the BCC Defect Analysis (BDA) algorithm [63], we attribute this anomalous negative stress to the formation of deformation twins within the ferrite phase in the 135° supercell. A detailed analysis of this phenomenon, however, lies beyond the scope of the present study. Tensile MD simulations are repeated three times, shown in black, red and blue, in order to verify reproducibility of the results.

The key features of these simulations are summarized in Fig. 6. Since the loading condition is not uniaxial, the so-called tensile modulus, defined as σ_1/ε_1, does not (exactly) correspond to the Young's modulus. In Fig. 6(a) the red squares and error bars represent the mean and standard deviation of the tensile modulus, measured at 1% strain, from three independent simulations as function of the loading direction. It shows that the modulus is highest at 0°(or equivalently 180°), reaching 274 GPa, while it is lowest at approximately 45° and 135°, dropping to about 190 GPa, 69% of the maximum value. The black solid line represents the tensile modulus calculated using the bicrystal model (Section 2) with a volume ratio of 4:1. The close agreement between the black line and the simulated values demonstrates the validity of the bicrystal model. The red solid line shows the calculated modulus for a volume ratio of 8:1, which corresponds to actual pearlite. The 8:1 ratio exhibits slightly larger fluctuations than the 4:1 case but the tensile modulus variation with loading direction is almost identical.

By taking the highest stress value in the near-linear phase of the tensile process as the yield strength, Fig. 6(b) illustrates the variation in yield strength across different loading directions. The yield strengths show a dramatic variation as function of loading direction, ranging from 9.5 GPa to 16.7 GPa. The yield strength reaches a maximum of 16.7 GPa at 0° and 90°. Interestingly, these directions correspond to the most extensively studied cases, and the 0° and 90° yield strengths are close to each other, which aligns well with previous reports [24,54]. Conversely, the minimum yield strength occurs at 45° and 135°—directions that were not considered in prior studies. Generally plastic deformation modes with lower yield strengths are assumed to be activated earlier during homogeneous deformation. Therefore, previous MD studies on the tensile behavior of pearlite appear to have overlooked the most probable deformation modes.

Fig. 6(c) shows the overall strain at which plastic deformation initiates in ferrite (red squares) and cementite (black squares), determined from observations of slip bands in the supercells. For ferrite, plastic deformation occurs latest under tensile loading along 0° and 90°, and earliest near 45° and 135°. Notably, in the 45° direction, plastic deformation begins at a strain of less than 6%. For cementite, plastic deformation is delayed the longest at 26° and 154° (above 10% strain), while it occurs earliest at 135° with a strain of 7.2%. Interestingly, for loading directions at 64° and 116°, plastic deformation in cementite occurs earlier than in ferrite—an observation not previously reported in MD simulations of pearlite deformation.

The tensile moduli along various directions are depicted in Fig. 6(a) shows a symmetry with respect to $(1\bar{1}0)_\alpha \| (100)_\theta$ plane. The strain corresponding to plasticity initiation shown in Fig. 6(c) does not exhibit such symmetry as explained in Section 2.2 based on the analysis of pearlite symmetry. In Fig. 6(b), the yield strength for various loading directions also seems to show such symmetry. It should be accidental, as the strain corresponding to the same yield strength and the plastic behavior within the two phases are not always consistent. Moreover, Fig. 5 shows that the stress strain curves for 26° and 154°, 45° and 135°, and 64° and 116° are similar but not identical.

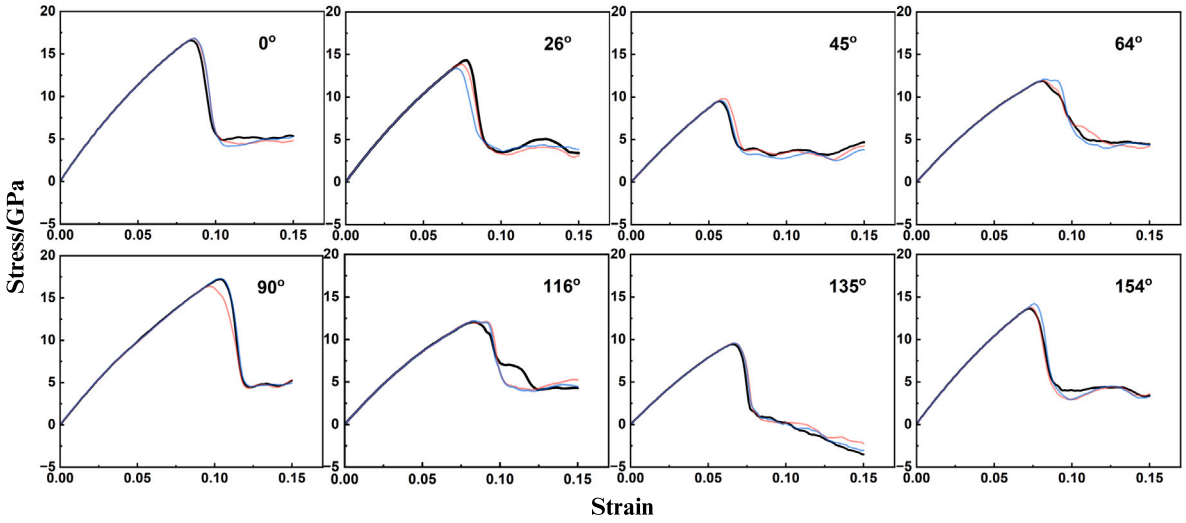

Fig. 5. Stress–strain curves for tensile deformation along eight different loading directions, with the specific direction labeled in each plot. Red and blue lines represent two replicates using different random seeds for initial velocity generation. (For interpretation of the references to color in this figure legend, the reader is referred to the web version of this article.)

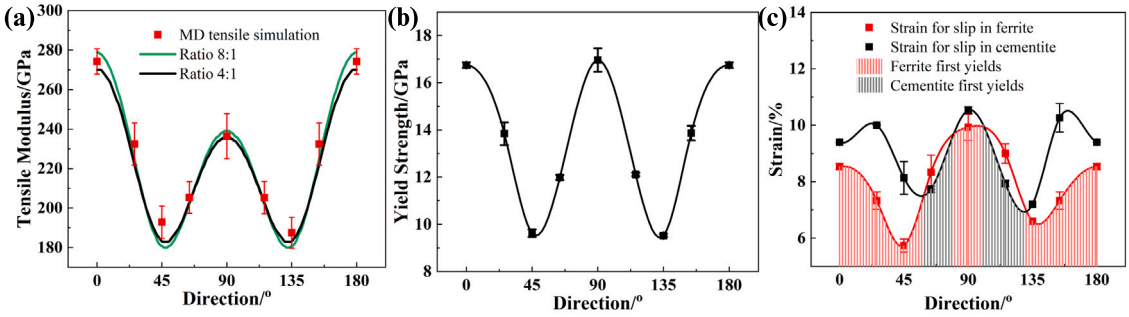

Fig. 6. (a) Tensile modulus and (b) yield strength for tensile deformation along eight different directions, as obtained from MD simulations. The tensile moduli predicted by the bicrystal model are also included in (a) for comparison. Error bars indicate the standard deviation from three independent simulations. (c) Strain at which slip initiates, marked by squares, in cementite (black) and ferrite (red). Regions where plastic deformation occurs first in ferrite (cementite) are highlighted with red (black) shading. Lines provide guides to the eye. (For interpretation of the references to color in this figure legend, the reader is referred to the web version of this article.)

4.2. Interfacial dislocation structure

Fig. 7 highlights the high-energy atoms near the interface (low energy atoms are made transparent for clarity), revealing the dislocation network formed due to lattice misfit.

The interfacial dislocations consist of two types of edge dislocations. The first type has dislocation lines parallel to $[010]_\theta \| [111]_\alpha$, with a Burgers vector $\mathbf{b}_1 = [110]_\alpha$ and a dislocation spacing p_1 of 40.3 Å. The second dislocation lines parallel to $[100]_\theta \| [1\bar{1}0]_\alpha$, with a Burgers vector $\mathbf{b}_2 = 1/2[111]_\alpha$ and a dislocation spacing p_2 of 81.5 Å. The pattern is identical to previous studies on the interface structure in pearlite with the Bagaryatskii OR [24,27]. The interfacial dislocation structure is the same for all equivalent supercells.

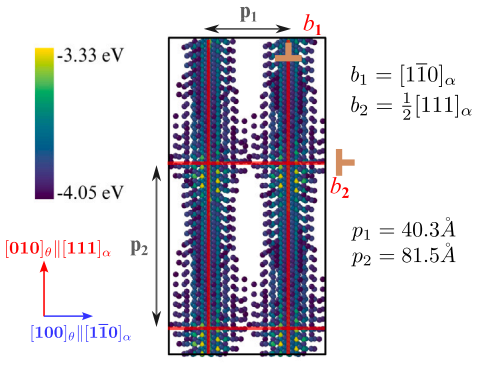

Fig. 7. Atoms with relatively high potential energy after relaxation are shown in the figure. The misfit dislocation pattern at ferrite/cementite interface is marked with red lines. The Burger's vectors and spacings of the two dislocations are labeled on the figure. (For interpretation of the references to color in this figure legend, the reader is referred to the web version of this article.)

4.3. Plasticity in ferrite

During the tensile simulation, the atomic configuration was recorded every 0.2% strain. The shear strain for each atom is calculated with initial configurations as references. Atoms with shear strains greater than 20% are considered to be the atoms that undergo plastic deformation. The planes formed by these atoms are regarded as slip planes, which are surrounded by dislocation lines (based on Dislocation Extraction Algorithm [64]). In the tensile simulations along various directions, five slip planes in ferrite at the initial stage of plasticity are observed, as shown in Figs. 8 (a-e). In these figures atoms belonging to the θ phase are colored gray. In the α phase only atoms with shear strain more than 20% are shown. The blue (white) atoms have a (non) BCC nearest neighbor shell according to common neighbor analysis. The schematic figure at upper right corner of each figure shows the position of the intersection lines of the slip plane at the interface (blue line) in relation to the misfit dislocation network (red line).

Table 4
Nominal Schmid factors m_n for slip systems which are observed in MD simulations at the initial stage of plasticity in ferrite. Angle 1 and 2 are the angles between the intersection of each slip plane with the two types of misfit dislocation lines on the interface. For each loading direction, the maximal m_n is highlighted in bold, and the actually activated slip planes are marked by underlining. The influence of incompatibility stress at the interface is taken into account.

Unit	Angle 1	Angle 2	0°	26°	45°	64°	90°	116°	135°	154°
	Degree		Dimensionless							
$(110)[\bar{1}11]$	90	0	0.287	**0.496**	0.403	0.237	0.058	0.112	0.077	0.066
$(110)[1\bar{1}1]$	90	0	0.287	0.066	0.077	0.112	0.058	0.237	0.403	**0.496**
$(1\bar{1}0)[111]$	0	90	0	0.381	**0.420**	0.402	0	0.402	**0.420**	0.381
$(121)[1\bar{1}1]$	73	17	**0.338**	0.076	0.167	0.306	0.310	0.128	0.352	0.468
$(211)[\bar{1}11]$	73	17	**0.338**	0.468	0.352	0.128	0.310	0.306	0.167	0.076
$(101)[\bar{1}11]$	59	31	0.298	0.315	0.207	0.015	0.479	**0.418**	0.212	0.066
$(011)[1\bar{1}1]$	59	31	0.298	0.066	0.212	**0.418**	0.479	0.015	0.207	0.315
$(1\bar{1}\bar{2})[1\bar{1}1]$	39	51	0.178	0.039	0.201	0.417	**0.519**	0.155	0.007	0.078
$(1\bar{1}2)[\bar{1}11]$	39	51	0.178	0.078	0.007	0.155	**0.519**	0.417	0.201	0.039

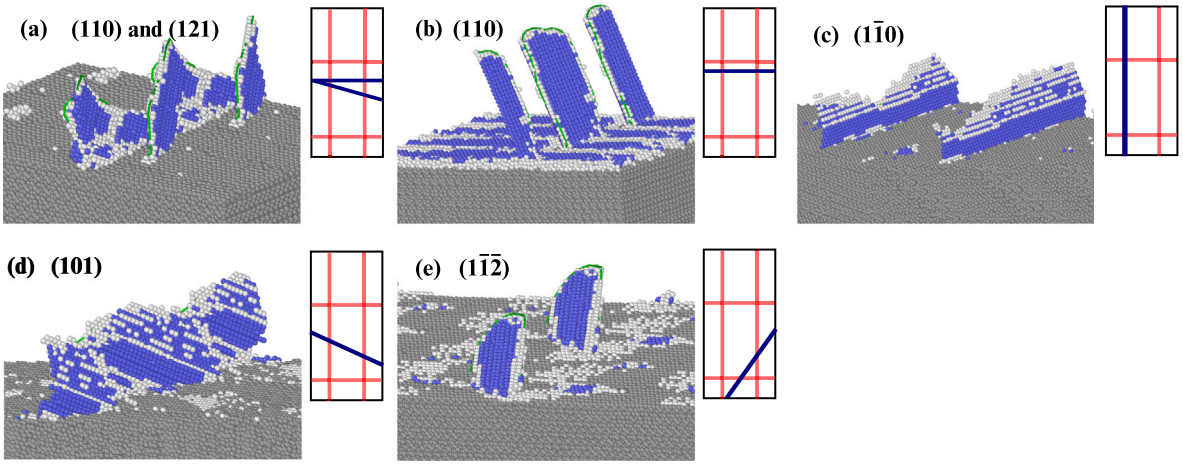

Fig. 8. Four types of slip plane found in ferrite. (a) A combination of (110) and (121) planes; (b) (110) plane; (c) $(1\bar{1}0)$ plane, and (d) $(1\bar{1}\bar{2})$ plane. The OR between observed slip plane-interface intersection (blue lines) and the misfit dislocations at the interface (red lines) are shown in each subplot. (For interpretation of the references to color in this figure legend, the reader is referred to the web version of this article.)

The nominal Schmid factors m_n of each slip system under various loading conditions were calculated using the model presented in Section 2, as summarized in Table 4. The actual relative external stress for each loading mode is shown in Table 3. For each loading direction, the highest m_n is highlighted in bold, and slip systems observed in the simulations are underlined. Angle 1 and angle 2 denote the angles between the intersection lines of slip planes with the interface and the initial interfacial dislocation lines $\mathbf{b}_1$ and $\mathbf{b}_2$, respectively. The activation of slip systems in ferrite has been experimentally studied [65] with microtensile tests. It was found that $\{110\}\langle 111\rangle$ and $\{112\}\langle 111\rangle$ have similar critical resolved shear stresses(CRSS) [65]. Therefore slip systems with high m_n are considered more likely to be activated in ferrite.

The $(110)_\alpha$ and $(1\bar{1}0)_\alpha$ slip planes are of particular interest. Their intersection lines at the interface are parallel to the initial dislocation network with Burgers vectors $\mathbf{b}_1$ and $\mathbf{b}_2$. In addition, due to the pearlite structural symmetry discussed in Section 3, the m_n for slip planes in the table show a certain symmetry with respect to the row of 90°. E.g. the m_n for loading angles $90° + \beta°$ for the $(110)[\bar{1}11]$ slip system are equal to the m_n for loading angles $90° - \beta°$ for the $(110)[1\bar{1}1]$ slip system.

For loading along 0° ($[010]_\theta \| [111]_\alpha$), the slip planes are $(110)_\alpha$ and $(121)_\alpha$. The m_n are relatively low, therefore external stress required for slip activation is high. For the 26° supercell, the m_n for the two planes are getting higher,leading to a drop in the yield strength. When loaded along 45°, both $(110)_\alpha$ and $(1\bar{1}0)_\alpha$ planes exhibit high m_n. However, surprisingly, slip occurs on the $(110)_\alpha$ plane only. Under 135° loading both the $(110)_\alpha$ and the $(1\bar{1}0)_\alpha$ planes have the same m_n as under 45° loading. Nevertheless, under 135° loading slip occurs extensively on the $(1\bar{1}0)_\alpha$ plane rather than on the $(110)_\alpha$ plane. This surprisingly distinct yielding behavior under 45° and 135° is evident by the red symbols in Fig. 6(c).

Considering the symmetry of pearlite discussed in Section 3, the onset of yielding and its progression is dependent on the symmetry properties of the whole supercell and on the atomic-scale structure.

For 64°, $(1\bar{1}0)_\alpha$ is the main slip surface although it has a lower m_n than $(011)_\alpha$. Slip on $(011)_\alpha$ is observed also, which has a higher m_n but a larger angle to the initial dislocation. When loading along 90° ($[100]_\theta \| [1\bar{1}0]_\alpha$), the m_n on both $(110)_\alpha$ and $(\bar{1}10)_\alpha$ slip surfaces are close to 0. $(1\bar{1}\bar{2})_\alpha$ and $(1\bar{1}2)_\alpha$ slip planes, which have the highest m_n, are activated. The cases of 116° and 154° supercells are consistent with the cases of 64° and 26° supercells, respectively.

A few key features of slip activity in ferrite are identified by combining observations of slip planes with m_n calculations:

(i) Consistency with previous studies: Shimokawa et al. [27] and Zhang et al. [54] reported that under tensile loading along $[100]_\theta \| [1\bar{1}0]_\alpha$, the $\{112\}\langle 111\rangle$ slip system is activated, while for loading along $[010]_\theta \| [111]_\alpha$, the $\{110\}\langle 111\rangle$ slip system dominates deformation. The slip planes observed in this study align well with these earlier findings, validating the current modeling approach.

(ii) Significance of nominal Schmid factor: For different loading directions, the slip systems with the highest m_n are generally activated. However, for the 45° case, the slip system with the second-highest m_n is activated instead.

(iii) Alignment with initial dislocation network: Slip planes with intersection lines parallel to the initial dislocation at the interface, such as (110) and $(1\bar{1}0)$, exhibit higher activity. For every loading direction studied, at least one active slip plane aligns with the initial dislocation. An exception is in the 90° case, where the m_n for the (110) and $(1\bar{1}0)$ slip planes are nearly zero. Then,

Table 5
Critical resolved shear stress for slip planes in ferrite calculated according to Eq. (13). Numbers marked with an asterisk correspond to the plastic deformation initiating in cementite, see Fig. 6(c).

	0°	26°	45°	64°	90°	116°	135°	154°
Slip plane 1	(110)	(110)	(110)	$(1\bar{1}0)$	$(1\bar{1}2)$	$(1\bar{1}0)$	$(1\bar{1}0)$	(110)
CRSS (GPa)	4.81	6.86	3.88	4.82*	8.80	4.87*	4.00	6.88
Slip plane 2	(121)	(211)		(011)		(101)		(121)
CRSS (GPa)	5.66	6.47		5.00*		5.06*		6.49

slip occurs on $(1\bar{1}2)$ and $(1\bar{1}\bar{2})$ planes. For the 0°, 64°, and 116° loading directions, (110) and $(1\bar{1}0)$ slip planes are observed, while other slip systems with slightly higher m_n remain inactive.

From the tensile simulation, CRSS for slip systems in ferrite are calculated using

$$\sigma^{\mathrm{CRSS}} = \sigma^{\mathrm{yield}} \cdot m_n, \tag{13}$$

where σ^{yield} is the yield strength shown in Fig. 6(b) and m_n is shown in Table 4. The CRSS values for all activated slip systems in ferrite are provided in Table 5. In general, the CRSS for $\{110\}_\alpha$ and $\{112\}_\alpha$ planes are comparable, as observed for loading directions of 0°, 26°, and 154°, consistent with experimental observations [65]. However, a notable exception is the $(1\bar{1}\bar{2})_\alpha$ plane under 90° loading, which exhibits a significantly higher CRSS of 8.80 GPa compared to other $\{112\}_\alpha$ planes. This highlights the critical influence of slip system alignment with interface dislocations in reducing the CRSS. For the $(110)_\alpha$ plane, the CRSS varies from 3.88 GPa (45° loading) to 6.88 GPa (154° loading). This variation arises from changes in the local atomic environment induced by significant, loading direction dependent, elastic deformation before slip initiation. It should be noted that the elastic strain exceeds 6% before yielding.

4.4. Plasticity in cementite

As shown in Fig. 9, the deformation of cementite, while straining pearlite supercells, can be categorized in three types,

(I) slip bands in cementite appear after significant plastic deformation in ferrite. E.g., Fig. 9(a) shows slip bands in the 0° supercell under 10% tensile strain, where a certain alignment between the slip planes in cementite and ferrite is observed. Slip transmission across the interface driven by strong plasticity in ferrite is reported previously as well [27,28].
(II) slip bands in cementite are activated shortly after plastic deformation begins in ferrite, as shown in Fig. 9(b). Strong correspondence of slip planes at two sides of the interface is observed.
(III) slip bands in cementite appear before plastic deformation in ferrite occurs, as shown in Fig. 9(c).

The slip planes observed during the initial stage of cementite plastic deformation under various loading conditions and their corresponding strain values are summarized in Table 6.

The cementite slip bands can be classified into two types according to their intersection lines at the $\theta - \alpha$ interface.

(i) $(0kl)_\theta$ slip bands with an intersection line of $[100]_\theta \| [1\bar{1}0]_\alpha$ at the interface.
(ii) $(h0l)_\theta$ slip bands with an intersection line of $[010]_\theta \| [111]_\alpha$ at the interface.

Slip planes in ferrite and slip bands in cementite are observed to form matching pairs: for supercells where the $(110)_\alpha$ slip plane is activated in ferrite, cementite exhibits $(0kl)_\theta$ slip bands, while when the $(1\bar{1}0)_\alpha$ slip plane is active in ferrite, cementite displays $(h0l)_\theta$ slip bands. The specific slip plane that occurs in ferrite as a function of the loading angle is given in Table 4.

Computational works, such as those by Karkina et al. [66,67], have shown that the stacking fault energy for different slip systems in cementite varies a lot. For example, the energy for stable stacking faults in $(103)_\theta$ is 0.28 J m^{-2} while for $(102)_\theta$ the value is 0.87 J m^{-2} [67]. Although the interatomic potential used previously [67] differs from the one applied in this work, here too, there is strong variation in the difficulty of initiating slip on various slip planes within cementite. Therefore, m_n for various slip systems in cementite are not a good indicator for the propensity of slip activation. Previous experiments [11,12] have suggested $[100]_\theta$ ($[010]_\theta$) is the slip direction for $(011)_\theta$ ($(101)_\theta$) slip planes. In this study, we adopt these directions for the $(0kl)_\theta$ and $(h0l)_\theta$ slip planes. This choice can be rationalized by the fact that slip systems with shorter Burgers vectors generally exhibit lower energy barriers during slip. Consequently, m_n for these slip systems are close to zero for the 0° and 90° loading cases but reach relatively high values for the 45° and 135° cases, as illustrated in Fig. 2(b).

To illustrate the influence of interfaces and incompatibility stresses on the activation of slip systems in cementite, we directly compare the deformation behavior of the cementite phase within pearlite with that of pure cementite under the same loading direction, as shown in Fig. 10. The tensile direction is 116°, corresponding to Type III deformation mode of pearlite in Fig. 9, in which slip occurs first in cementite. The slip planes were identified as atoms with shear strain greater than 0.2. Fig. 10(a) and (b) show the slip planes of cementite in pearlite and bulk cementite, respectively. In (a), slip occurs at a strain of 8.4%, while in (b), the value is 13.4%. For bulk cementite, the slip planes are $(201)_\theta$ and $(\bar{2}01)_\theta$, which can be inferred as the most favorable slip planes under this loading condition. Multiple slip planes are formed simultaneously. In contrast, for cementite within pearlite, slip occurs on the $(201)_\theta$ and $(203)_\theta$ planes. Compared to bulk cementite, on one hand, the slip planes in pearlite originate from interfacial dislocations and are fewer in number; on the other hand, they include both the (201) plane, consistent with bulk cementite, and the $(203)_\theta$ plane, which forms to maintain compatibility with interfacial dislocations.

Fig. 10(c) shows the stress–strain curves for pearlite and cementite under the same loading condition. Three independent simulations for bulk cementite were performed with different random initial velocities to ensure consistency. For ferrite and cementite in pearlite, the stresses are represented by red and blue dots, respectively, obtained by averaging the stresses of atoms located at least 5 Å away from the interface in each phase. Key observations include:

(i) The stress required for slip in cementite within pearlite is 13.8 GPa, whereas for bulk cementite it is approximately 40% higher at 19.3 GPa.
(ii) In pearlite deformation, the two phases bear different stress levels. Ferrite, with a lower tensile modulus, exhibits lower stress (red dots), while cementite exhibits higher stress (blue dots). Even after substantial elastic deformation when the two phases are no longer in the linear elastic regime, the cementite still bears the higher tensile stress.
(iii) The model shown in Section 2 predicts the stresses in the two phases during deformation, as shown by the two dashed lines. At low strains, the predicted values agree well with the MD simulation. At higher strains, although the material remains in the elastic regime, the stress–strain relationship becomes nonlinear, and the MD stress levels are lower than the predicted values.
(iv) Compared to bulk cementite, cementite within pearlite exhibits higher stress at the same strain, as predicted by the analytical model, which shows the influence of incompatibility stresses. The contribution of incompatibility stresses exists throughout the elastic regime. When the overall strain exceeds 6%, the stress in cementite within pearlite becomes lower than that in bulk cementite due to interface sliding.

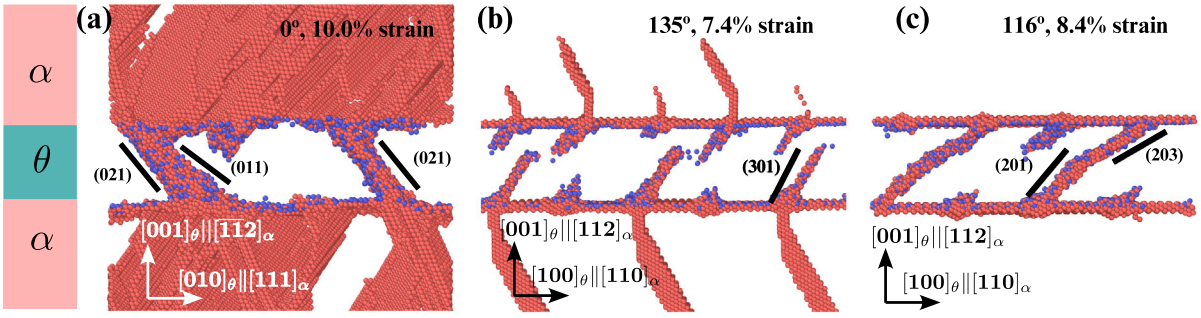

Fig. 9. Three types of slip planes observed in cementite. (a) Type I: slip systems in cementite are activated after significant plastic deformation in ferrite. (b) Type II: slip planes in ferrite and cementite are activated synchronously, exhibiting identical slip traces at the interface. (c) Type III: slip occurs first in cementite. The classifications for various loading conditions are listed in Table 6. Fe (C) atoms with a shear strain of more than 20% are colored in red (blue) while atoms with less than 20% shear strain are not shown. The perspectives of the three figures correspond to the directions along $[100]_\theta$ and twice $[010]_\theta$. Animations corresponding to the three types of plastic deformation are provided in Supplement 1. (For interpretation of the references to color in this figure legend, the reader is referred to the web version of this article.)

Table 6
Slip planes observed during the initial stage of plastic deformation in cementite under various loading conditions. The strain values required to activate these slip planes, averaged over three independent simulations, are listed also. For loading directions where slip occurs in cementite first, the CRSS is calculated according to Eq. (13).

Loading condition	0°	26°	45°	64°	90°	116°	135°	154°
Slip plane	(021) (011) $(0\bar{2}1)$	(021) (031)	(021) (031)	$(20\bar{1})$ $(10\bar{1})$	$(20\bar{1})$ $(10\bar{1})$ (101)	(201) (101)	(201) (301)	(011) (032)
Corresponding Strain (%)	9.4	10.0	8.1	7.7	10.5	7.9	7.2	10.3
Relation to Slip in ferrite	I	I	I	II, III	I	III	II	I
CRSS (GPa)				4.1		4.2	5.8	

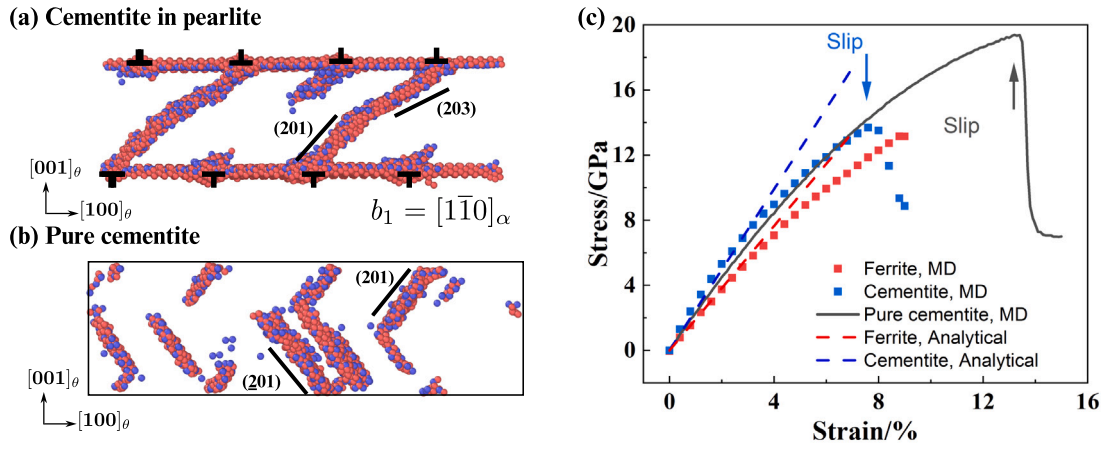

Fig. 10. Comparison of tensile deformation in cementite embedded in pearlite and pure cementite. (a) Slip bands in cementite as part of pearlite, loaded along the 116° direction at an overall strain of 8.4%. (b) Slip bands in bulk cementite under same loading direction as (a), at a strain of 13.4%. (c) Stress–strain curves for the two supercells. For ferrite and cementite in pearlite, the stresses are represented by red and blue dots, respectively, while the black line represents the stress–strain relation in bulk cementite. The stress is obtained by averaging the σ_1 atomic stress component of atoms located at least 5 Å away from the interface in each phase. The theoretical stresses in the two phases, calculated using the analytical model in Section 2, are shown as dashed lines. (For interpretation of the references to color in this figure legend, the reader is referred to the web version of this article.)

In brief, the lower slip stress in cementite within pearlite at this loading direction is attributed to three factors: the higher tensile modulus of cementite relative to ferrite, stress concentration caused by interfacial incompatibility stresses, and the facilitation of slip by interfacial dislocations. For the case of loading along 116°, Fig. 10(c) demonstrates that the dislocations near the interface initiate slip in cementite at lower stresses than in bulk cementite.

5. Discussion

5.1. Factors influence the plasticity in pearlite

In this paper, the effect of the loading direction on the deformation behavior of pearlite is demonstrated using equivalent supercells with carefully designed periodicities. The analytical model in Section 2 gives insight in the elastic properties of pearlite and considers the nominal Schmid factors m_n in both the ferrite and cementite constituents. On the basis of m_n, the onset of plastic deformation can be guessed, however, our MD simulations reveal that such a description is oversimplified. There are various factors affecting the deformation of pearlite.

(i) Nominal Schmid factors m_n. m_n aligns closely with the activation of slip systems. For ferrite, the Schmid factor provides a quantitative prediction of the activated slip planes, as found previously also [25]. For cementite, the magnitude of m_n qualitatively explains the influence of the loading direction on slip activation. For loading directions with high m_n in cementite (e.g., 45° and 135°), slip planes in cementite are activated at strains of 8.1%

and 7.2%, respectively. In contrast, for directions with low m_n in cementite (e.g., 0° and 90°), slip activation occurs at strains of 9.4% and 10.5%, respectively, showing a significant increase.

(ii) Interfacial dislocations. The initial interfacial dislocation structure reduces the critical resolved shear stress (CRSS), enabling slip planes parallel to the interfacial dislocation lines to activate earlier, here: $(110)_\alpha$ and $(1\bar{1}0)_\alpha$. The CRSS for ferrite slip can be estimated by dividing the yield strength by m_n of the activated slip system. For the $(1\bar{1}2)_\alpha$ plane, which has a 39° angle with interfacial dislocations, the CRSS is 8.8 GPa. For the $(110)_\alpha$ slip plane along the dislocation line, the CRSS is only 4.8 GPa, 45% less than for $(1\bar{1}2)_\alpha$. When loading at 0°, the initial slip occurs on the $(110)_\alpha$ plane. This plane aligns with the interfacial dislocation $\mathbf{b}_2$. The $(121)_\alpha$ plane, which has a higher m_n but is not as well aligned with interfacial dislocations, slips subsequently. For cementite, the $[010]_\theta$ and $[100]_\theta$ directions are aligned with the interfacial dislocation lines. Therefore the intersection lines of $(0kl)_\theta$ and $(h0l)_\theta$ planes on the interface is parallel to the interfacial dislocation. It can be expected that this specific orientation facilitates a lower energy barrier for slip activation in cementite.

(iii) Loading direction. The loading direction significantly influences the m_n. In pure ferrite, the abundance of slip systems results in relatively low m_n anisotropy. However, in pearlite, the interfacial dislocations reduce the CRSS for $(110)_\alpha$ and $(1\bar{1}0)_\alpha$ planes, introducing pronounced anisotropy in ferrite slip activation. For cementite, the limited number of slip systems causes substantial anisotropy in m_n, as shown in Fig. 2(b).

(iv) Volume ratio of the two phases. While phase volume fractions do not directly alter the geometric relationship between interface structure and slip systems, they strongly affect the distribution of incompatibility stresses at the interface. The stress partitioning is inversely proportional to the phase volume fraction, leading to significant stress concentrations in the phase with smaller volume, as shown in Fig. 3(a). In pearlite with a ferrite-to-cementite volume ratio of 8 : 1, this amplifies the anisotropy of slip activation in cementite.

(v) Temperature. During the tensile simulations, the temperature was maintained at 300 K using a Nose–Hoover thermostat. This temperature is significantly higher than that used in previous MD simulations [24,25,27]. Given that the plasticity of cementite is highly temperature-sensitive [9], this elevated temperature may explain the occurrence of slip bands in this work. From a practical perspective, the actual wire drawing process of pearlite involves large plastic deformation, which results in substantial heat accumulation. Takahashi et al. [68] demonstrated that reducing the drawing speed to mitigate thermal effects can suppress the decomposition of cementite. Therefore, the temperature setting in MD simulations warrants careful consideration in order to accurately represent realistic thermal conditions during pearlite processing.

5.2. Insights into the anisotropy of plastic deformation in pearlite

The current analysis shows a significant dependence of the plasticity of pearlite on the loading direction, which arises from factors such as the lamellar structure, initial dislocations at interfaces, and the geometric relationship between the loading direction and slip systems. We hypothesize that the deformation mechanism of pearlite proceeds as follows:

In the earliest stages of deformation, ferrite with favorably oriented slip systems deforms first and undergoes work hardening through dislocation multiplication. The plastic deformation is highly localized, as observed in experiments [18,20,69]. This explains the relatively low yield strength of pearlite, as shown in pearlite tensile tests [69].

Subsequently, cementite in geometrically favorable orientations begins to slip with the assistance of interfacial dislocations. This challenges the view that cementite plasticity is caused only by dislocation pile-up in ferrite at the interface [24,25,28,57]. By examining a wider range of loading directions, we find that the tensile stress needed for slip behavior in cementite can be less than 10 GPa, which is much lower than previous studies, for example, 12–19 GPa from first principles calculation [47] and 15–20 GPa from MD simulation [24]. The loading direction selected in previous studies [24,27,28,54,57] corresponds to a relatively low m_n in cementite, as shown in Fig. 2, which explains the high external stresses that are required for activation of slips in cementite in these works. The predicted early onset of cementite slip suggests that cementite fragmentation and amorphization observed in experiments [13,69] could occur at the initial stages of pearlite drawing. Interfacial dislocations also emit dislocations into the ferrite. The geometrically connected slip planes on both sides of the interface facilitate the relocation of carbon atoms from cementite to ferrite [15,70]. This carbon relocation enhances the work-hardening rate in ferrite, which in turn maintains the load-carrying capacity of the material and prevents necking instability during severe plastic deformation.

For cementite with geometrically unfavorable orientation, dislocations originating in the adjacent ferrite accumulate at the interfaces and eventually penetrate into the cementite, as described previously [24,25,28,57]. This process represents a secondary strengthening mechanism that becomes active as deformation continues. As the thickness of cementite layer decreases, stress concentration within the cementite becomes more pronounced, as discussed in Section 2.1. This mechanism further promotes cementite decomposition and enhances solid-solute strengthening in ferrite.

Several key characteristics of pearlite are crucial for achieving exceptional work-hardening rate increases as a function of strain.

(i) The presence of (semi-)coherent interfaces ensures interfacial strength and facilitates slip transfer.

(ii) The low volume fraction and the very fine lamellar distribution of the brittle phase allow it to undergo slip without crack formation when embedded in a deformable phase.

(iii) The brittle phase can decompose, releasing a large number of interstitial solute atoms, leading to strengthening through the coupling of dislocations and solute atoms during deformation.

(iv) The significant variation in yield strength among domains with different stacking orientations contributes to the ability to achieve large plastic deformation before failure.

Many eutectic and eutectoid alloys have finely layered microstructures, resembling pearlite, suggesting that there may be other alloys where high strength and plasticity can be achieved [71–74]. For example, Chen et al. [75] applied heavy drawing to a eutectic high-entropy alloy wire with a FCC-B2 structure. After severe deformation, the wire showed excellent strength while maintaining good ductility.

Previous studies have emphasized the importance of ψ, the angle between the loading direction and the pearlite stacking direction, in analyzing pearlite deformation [18,55,76]. For example, Toshihiko et al. investigated the relationship between the strain within a pearlite colony and ψ [76]. However, this work demonstrates that even when the loading direction lies within the plane of the α-θ interface, the mechanical properties and deformation mechanisms of pearlite exhibit significant variation, as shown in Fig. 6. For a general ψ, the pearlitic orientations corresponding to a specific angle form a conical surface in three-dimensional space. In Fig. 2, points on circles centered at the origin of the XOZ stereographic projection represent the same ψ. m_n (indicated by color) vary widely across these orientations. This variation highlights the inadequacy of classification methods based solely on the angle between the loading direction and the stacking direction. Moreover, in real materials, plastic deformation is governed by regions that yield first, making deformation modes with lower yield strengths more relevant. Therefore, for structurally anisotropic materials like pearlite, a careful selection of loading directions is crucial to ensure representative results in simulations and micro-mechanical experiments.

6. Conclusion

In this study, molecular dynamics simulations combined with an analytical model are employed to investigate the deformation behavior of pearlite. For the Bagaryatskii orientation relationship, we find that the loading directions chosen in previous studies do not adequately represent the actual deformation mechanism of pearlite. To allow a wide range of loading directions in atomically identical supercells, tensile simulations are conducted using equivalent supercells with carefully designed periodicities. As during wire-drawing lamellae are observed to align with the drawing direction, various loading directions perpendicular to the stacking direction were examined. The main conclusions are as follows.

(i) Pearlite exhibits significant anisotropy in plastic deformation capacity. Even when the loading direction is within the interface plane, the yield strength varies greatly with the angle between the loading direction and the $[010]_\theta$ direction, ranging from a minimum of 9.5 GPa at 45° and 135° to a maximum of 17.0 GPa at 0° and 90°.

(ii) In certain loading directions, slip bands in cementite activate before ferrite, challenging the conventional assumption that deformation always starts in ferrite and then transfers to cementite. A sequence of strengthening mechanisms – initial work hardening in ferrite, slip in favorably oriented cementite, and slip transfer into unfavorably oriented cementite – coupled with interfacial effects and carbon dissolution, results in work hardening over a wide range of strain, explaining the remarkable plastic deformation and exceptional tensile strength.

(iii) During early-stage deformation, slip systems in both phases align with initial interfacial dislocations. Slip activation in ferrite is according to the nominal Schmid factor m_n. At specific loading directions, and during later stages of deformation, slip initiation in cementite occurs. This is promoted by the low cementite volume fraction and by high temperature.

The approach presented here is applicable to other lamellar alloy systems. By leveraging the structural and processing insights from pearlite, it is anticipated that other materials with superior deformability and high strength can be developed.

CRediT authorship contribution statement

Kai Liu: Writing – original draft, Visualization, Validation, Software, Methodology, Investigation, Funding acquisition, Formal analysis, Data curation, Conceptualization. **Fei Shuang:** Formal analysis, Data curation. **Marcel H.F. Sluiter:** Writing – review & editing, Supervision, Project administration, Funding acquisition, Conceptualization.

Declaration of competing interest

The authors declare that they have no known competing financial interests or personal relationships that could have appeared to influence the work reported in this paper.

Acknowledgments

The authors acknowledge discussions with Profs. Kestens and Sietsma of Ghent and Delft University, respectively. One of the authors, KL, gratefully acknowledges financial support from the China Scholarship Council, China (CSC, No. 202006120016). This publication is partly financed by the Dutch Research Council (NWO) under the grant EINF-9662.

Appendix A. Supplementary materials

Supplementary material related to this article can be found online at https://doi.org/10.1016/j.actamat.2025.121100.

References

[1] Y. Li, D. Raabe, M. Herbig, P.-P. Choi, S. Goto, A. Kostka, H. Yarita, C. Borchers, R. Kirchheim, Segregation stabilizes nanocrystalline bulk steel with near theoretical strength, Phys. Rev. Lett. 113 (10) (2014) 106104.
[2] X. Zhang, A. Godfrey, N. Hansen, X. Huang, W. Liu, Q. Liu, Evolution of cementite morphology in pearlitic steel wire during wet wire drawing, Mater. Charact. 61 (1) (2010) 65–72.
[3] S. Djaziri, Y. Li, G.A. Nematollahi, B. Grabowski, S. Goto, C. Kirchlechner, A. Kostka, S. Doyle, J. Neugebauer, D. Raabe, G. Dehm, Deformation-induced martensite: A new paradigm for exceptional steels, Adv. Mater. 28 (35) (2016) 7753–7757, http://dx.doi.org/10.1002/adma.201601526.
[4] X. Zhang, A. Godfrey, X. Huang, N. Hansen, Q. Liu, Microstructure and strengthening mechanisms in cold-drawn pearlitic steel wire, Acta Mater. 59 (9) (2011) 3422–3430.
[5] C. Borchers, R. Kirchheim, Cold-drawn pearlitic steel wires, Prog. Mater. Sci. 82 (2016) 405–444.
[6] J.J. Coronado, S.A. Rodríguez, Cementite characterization with chromium and vanadium contents using indentation technique, J. Iron Steel Res. Int. 22 (4) (2015) 366–370.
[7] A. Fernández-Vicente, M. Pellizzari, J. Arias, Feasibility of laser surface treatment of pearlitic and bainitic ductile irons for hot rolls, J. Mater. Process. Technol. 212 (5) (2012) 989–1002.
[8] J. Alkorta, J.G. Sevillano, Assessment of elastic anisotropy and incipient plasticity in Fe_3C by nanoindentation, J. Mater. Res. 27 (1) (2012) 45–52.
[9] T. Terashima, Y. Tomota, M. Isaka, T. Suzuki, M. Umemoto, Y. Todaka, Strength and deformation behavior of bulky cementite synthesized by mechanical milling and plasma-sintering, Scr. Mater. 54 (11) (2006) 1925–1929.
[10] H. Tsybenko, C. Tian, J. Rau, B. Breitbach, P. Schreiber, C. Greiner, G. Dehm, S. Brinckmann, Deformation and phase transformation in polycrystalline cementite (Fe_3C) during single-and multi-pass sliding wear, Acta Mater. 227 (2022) 117694.
[11] A. Inoue, T. Ogura, T. Masumoto, Deformation and fracture behaviours of cementite, Trans. Japan Inst. Met. 17 (10) (1976) 663–672.
[12] A. Inoue, T. Ogura, T. Masumoto, Burgers vectors of dislocations in cementite crystal, Scr. Metall. 11 (1) (1977) 1–5.
[13] Y. Zhou, X. Shao, S. Zheng, X. Ma, Structure evolution of the Fe_3C/Fe interface mediated by cementite decomposition in cold-deformed pearlitic steel wires, J. Mater. Sci. Technol. 101 (2022) 28–36.
[14] Y. Li, P. Choi, C. Borchers, S. Westerkamp, S. Goto, D. Raabe, R. Kirchheim, Atomic-scale mechanisms of deformation-induced cementite decomposition in pearlite, Acta Mater. 59 (10) (2011) 3965–3977.
[15] P.-Y. Tung, X. Zhou, D. Mayweg, L. Morsdorf, M. Herbig, Under-stoichiometric cementite in decomposing binary Fe-C pearlite exposed to rolling contact fatigue, Acta Mater. 216 (2021) 117144.
[16] A. Kanie, Y. Tomota, S. Torii, T. Kamiyama, Elastic strains of cementite in a pearlite steel during tensile deformation measured by neutron diffraction, ISIJ Int. 44 (11) (2004) 1952–1956.
[17] E. Gadalińska, A. Baczmański, C. Braham, G. Gonzalez, H. Sidhom, S. Wroński, T. Buslaps, K. Wierzbanowski, Stress localisation in lamellar cementite and ferrite during elastoplastic deformation of pearlitic steel studied using diffraction and modelling, Int. J. Plast. 127 (2020) 102651.
[18] Y. Yajima, N. Koga, C. Watanabe, Influential factors on the deformability of colonies in pearlitic steel, Mater. Charact. 177 (2021) 111197.
[19] P.B.P. Leão, J.R.B. Neto, S.F. Rodrigues, L. Novotnỳ, J.L. Cardoso, L.F.G. Herculano, T.N. Lima, A.J. Ramirez, H.F.G. de Abreu, In-situ tensile-shear test in SEM and DIC analysis of two pearlitic steel microstructures: undeformed-coarse and deformed-refined, J. Mater. Res. Technol. 24 (2023) 9441–9461.
[20] M. Tanaka, Y. Yoshimi, K. Higashida, T. Shimokawa, T. Ohashi, A multiscale approach for the deformation mechanism in pearlite microstructure: Experimental measurements of strain distribution using a novel technique of precision markers, Mater. Sci. Eng.: A 590 (2014) 37–43.
[21] K.O. Henriksson, K. Nordlund, Simulations of cementite: An analytical potential for the Fe-C system, Phys. Rev. B— Condens. Matter Mater. Phys. 79 (14) (2009) 144107.
[22] L.S. Liyanage, S.-G. Kim, J. Houze, S. Kim, M.A. Tschopp, M.I. Baskes, M.F. Horstemeyer, Structural, elastic, and thermal properties of cementite (Fe_3C) calculated using a modified embedded atom method, Phys. Rev. B 89 (9) (2014) 094102.
[23] M. Guziewski, S.P. Coleman, C.R. Weinberger, Interface energetics and structure of the pearlitic microstructure in steels: An atomistic and continuum investigation, Acta Mater. 155 (2018) 1–11.
[24] M. Guziewski, S.P. Coleman, C.R. Weinberger, Atomistic investigation into the mechanical properties of the ferrite-cementite interface: The bagaryatskii orientation, Acta Mater. 144 (2018) 656–665.
[25] M. Guziewski, S.P. Coleman, C.R. Weinberger, Atomistic investigation into interfacial effects on the plastic response and deformation mechanisms of the pearlitic microstructure, Acta Mater. 180 (2019) 287–300.
[26] M. Yu, F. Duan, Atomistic investigation of deformation behavior of lamellar pearlite with inclined orientation, Int. J. Plast. 177 (2024) 103988.

[27] T. Shimokawa, T. Niiyama, M. Okabe, J. Sawakoshi, Interfacial-dislocation-controlled deformation and fracture in nanolayered composites: Toward higher ductility of drawn pearlite, Acta Mater. 164 (2019) 602–617.

[28] L.-W. Liang, Y.-J. Wang, Y. Chen, H.-Y. Wang, L.-H. Dai, Dislocation nucleation and evolution at the ferrite-cementite interface under cyclic loadings, Acta Mater. 186 (2020) 267–277.

[29] H. Ghaffarian, A.K. Taheri, S. Ryu, K. Kang, Nanoindentation study of cementite size and temperature effects in nanocomposite pearlite: A molecular dynamics simulation, Curr. Appl. Phys. 16 (9) (2016) 1015–1025.

[30] I. Watanabe, D. Setoyama, N. Nagasako, N. Iwata, K. Nakanishi, Multiscale prediction of mechanical behavior of ferrite–pearlite steel with numerical material testing, Internat. J. Numer. Methods Engrg. 89 (7) (2012) 829–845.

[31] T. Richeton, S. Berbenni, Effects of heterogeneous elasticity coupled to plasticity on stresses and lattice rotations in bicrystals: A field dislocation mechanics viewpoint, Eur. J. Mech. A Solids 37 (2013) 231–247, http://dx.doi.org/10.1016/j.euromechsol.2012.06.010.

[32] T. Richeton, I. Tiba, S. Berbenni, O. Bouaziz, Analytical expressions of incompatibility stresses at $\Sigma 3 < 111 >$ twin boundaries and consequences on single-slip promotion parallel to twin plane, Phil. Mag. 95 (1) (2015) 12–31, http://dx.doi.org/10.1080/14786435.2014.984787.

[33] K. Liu, M.H. Sluiter, Incompatibility stress at inclined grain boundaries for cubic crystals under hydrostatic stress and uniaxial stress, Materialia 34 (2024) 102071, http://dx.doi.org/10.1016/j.mtla.2024.102071, URL https://www.sciencedirect.com/science/article/pii/S2589152924000681.

[34] K. Liu, M.H. Sluiter, Stresses at grain boundaries: The maximum incompatibility stress in an infinitely extended elastic bicrystal under uniaxial loading, Scr. Mater. 234 (2023) 115570, http://dx.doi.org/10.1016/j.scriptamat.2023.115570, URL https://www.sciencedirect.com/science/article/pii/S1359646223002944.

[35] Y.A. Bagaryatskii, The probable mechanism of the martensite decomposition (H. Brutcher Technical Translations), Dokl. Akad. Nauk SSSR 73 (1950) 1161–1164.

[36] W. Guo, Y. Meng, X. Zhang, V. Bedekar, H. Bei, S. Hyde, Q. Guo, G.B. Thompson, R. Shivpuri, J.-M. Zuo, et al., Extremely hard amorphous-crystalline hybrid steel surface produced by deformation induced cementite amorphization, Acta Mater. 152 (2018) 107–118.

[37] J. Wang, Z. Ma, G. Ding, R. Yang, S. Cai, L. Dai, M. Jiang, C. Lu, Energy dissipation in pearlitic steel under impact loading, Acta Mater. 284 (2025) 120599.

[38] C. Jiang, S.G. Srinivasan, A. Caro, S.A. Maloy, Structural, elastic, and electronic properties of Fe_3C from first principles, J. Appl. Phys. 103 (4) (2008) 043502, http://dx.doi.org/10.1063/1.2884529, arXiv:https://pubs.aip.org/aip/jap/article-pdf/doi/10.1063/1.2884529/15001337/043502_1_online.pdf.

[39] J.P. Perdew, Y. Wang, Accurate and simple analytic representation of the electron-gas correlation energy, Phys. Rev. B 45 (23) (1992) 244–249.

[40] J.P. Perdew, K. Burke, M. Ernzerhof, Generalized gradient approximation made simple, Phys. Rev. Lett. 77 (1996) 3865–3868, http://dx.doi.org/10.1103/PhysRevLett.77.3865.

[41] M. Sluiter, M. Weinert, Y. Kawazoe, Determination of the elastic tensor in low-symmetry structures, Europhys. Lett. 43 (2) (1998) 183, http://dx.doi.org/10.1209/epl/i1998-00338-1.

[42] J.A. Rayne, B.S. Chandrasekhar, Elastic constants of iron from 4.2 to 300 K, Phys. Rev. 122 (1961) 1714–1716, http://dx.doi.org/10.1103/PhysRev.122.1714.

[43] J.J. Adams, D. Agosta, R. Leisure, H. Ledbetter, Elastic constants of monocrystal iron from 3 to 500 K, J. Appl. Phys. 100 (11) (2006).

[44] M. Müller, P. Erhart, K. Albe, Analytic bond-order potential for bcc and fcc iron—comparison with established embedded-atom method potentials, J. Phys.: Condens. Matter. 19 (32) (2007) 326220, http://dx.doi.org/10.1088/0953-8984/19/32/326220.

[45] M. Nikolussi, S. Shang, T. Gressmann, A. Leineweber, E. Mittemeijer, Y. Wang, Z.-K. Liu, Extreme elastic anisotropy of cementite, Fe_3C: First-principles calculations and experimental evidence, Scr. Mater. 59 (8) (2008) 814–817, http://dx.doi.org/10.1016/j.scriptamat.2008.06.015, URL https://www.sciencedirect.com/science/article/pii/S1359646208004594.

[46] Z. Lv, F. Zhang, S. Sun, Z. Wang, P. Jiang, W. Zhang, W. Fu, First-principles study on the mechanical, electronic and magnetic properties of Fe_3C, Comput. Mater. Sci. 44 (2) (2008) 690–694, http://dx.doi.org/10.1016/j.commatsci.2008.05.006, URL https://www.sciencedirect.com/science/article/pii/S0927025608002449.

[47] N. Garvik, P. Carrez, P. Cordier, First-principles study of the ideal strength of Fe_3C cementite, Mater. Sci. Eng.: A 572 (2013) 25–29, http://dx.doi.org/10.1016/j.msea.2013.02.028, URL https://www.sciencedirect.com/science/article/pii/S0921509313001858.

[48] G. Ghosh, A first-principles study of cementite (Fe_3C) and its alloyed counterparts: Elastic constants, elastic anisotropies, and isotropic elastic moduli, AIP Adv. 5 (8) (2015) 087102, http://dx.doi.org/10.1063/1.4928208, arXiv:https://pubs.aip.org/aip/adv/article-pdf/doi/10.1063/1.4928208/8442669/087102_1_online.pdf.

[49] L. Mauger, J.E. Herriman, O. Hellman, S.J. Tracy, M.S. Lucas, J.A. Muñoz, Y. Xiao, J. Li, B. Fultz, Phonons and elasticity of cementite through the Curie temperature, Phys. Rev. B 95 (2017) 024308, http://dx.doi.org/10.1103/PhysRevB.95.024308.

[50] F. Roters, P. Eisenlohr, T.R. Bieler, D. Raabe, Crystal Plasticity Finite Element Methods: in Materials Science and Engineering, John Wiley & Sons, 2011.

[51] I. Tiba, T. Richeton, C. Motz, H. Vehoff, S. Berbenni, Incompatibility stresses at grain boundaries in Ni bicrystalline micropillars analyzed by an anisotropic model and slip activity, Acta Mater. 83 (2015) 227–238.

[52] S.-F. Chen, H.-W. Song, S.-H. Zhang, M. Cheng, C. Zheng, M.-G. Lee, An effective Schmid factor in consideration of combined normal and shear stresses for slip/twin variant selection of Mg-3Al-1Zn alloy, Scr. Mater. 167 (2019) 51–55.

[53] D. Xia, X. Chen, G. Huang, B. Jiang, A. Tang, H. Yang, S. Gavras, Y. Huang, N. Hort, F. Pan, Calculation of Schmid factor in Mg alloys: Influence of stress state, Scr. Mater. 171 (2019) 31–35.

[54] H. Zhang, Y. Chen, Y. Sun, Molecular dynamics simulation study on impact of interface chemistry on pearlite mechanical response, Mater. Res. Express 10 (9) (2023) 096514.

[55] A. Durgaprasad, S. Giri, S. Lenka, S. Kundu, S. Mishra, S. Chandra, R. Doherty, I. Samajdar, Defining a relationship between pearlite morphology and ferrite crystallographic orientation, Acta Mater. 129 (2017) 278–289.

[56] F. Fang, L. Zhou, X. Hu, X. Zhou, Y. Tu, Z. Xie, J. Jiang, Microstructure and mechanical properties of cold-drawn pearlitic wires affect by inherited texture, Mater. Des. 79 (2015) 60–67.

[57] H. Ghaffarian, A.K. Taheri, K. Kang, S. Ryu, Molecular dynamics simulation study on the effect of the loading direction on the deformation mechanism of pearlite, Multiscale Sci. Eng. 1 (2019) 47–55.

[58] T. Shimokawa, T. Oto, T. Niiyama, Molecular dynamics simulation of the effect of cementite decomposition on yield phenomena in pearlite microstructure, ISIJ Int. 62 (2) (2022) 343–352.

[59] A. Jain, S.P. Ong, G. Hautier, W. Chen, W.D. Richards, S. Dacek, S. Cholia, D. Gunter, D. Skinner, G. Ceder, et al., Commentary: The materials project: A materials genome approach to accelerating materials innovation, APL Mater. 1 (1) (2013).

[60] P. Hirel, Atomsk: A tool for manipulating and converting atomic data files, Comput. Phys. Comm. 197 (2015) 212–219.

[61] A.P. Thompson, H.M. Aktulga, R. Berger, D.S. Bolintineanu, W.M. Brown, P.S. Crozier, P.J. in 't Veld, A. Kohlmeyer, S.G. Moore, T.D. Nguyen, R. Shan, M.J. Stevens, J. Tranchida, C. Trott, S.J. Plimpton, LAMMPS - a flexible simulation tool for particle-based materials modeling at the atomic, meso, and continuum scales, Comp. Phys. Comm. 271 (2022) 108171, http://dx.doi.org/10.1016/j.cpc.2021.108171.

[62] A. Stukowski, Visualization and analysis of atomistic simulation data with OVITO-the open visualization tool, Modelling Simul. Mater. Sci. Eng. 18 (1) (2010) http://dx.doi.org/10.1088/0965-0393/18/1/015012.

[63] J.J. Möller, E. Bitzek, BDA: A novel method for identifying defects in body-centered cubic crystals, MethodsX 3 (2016) 279–288.

[64] A. Stukowski, V.V. Bulatov, A. Arsenlis, Automated identification and indexing of dislocations in crystal interfaces, Modelling Simul. Mater. Sci. Eng. 20 (8) (2012) 085007.

[65] C. Du, F. Maresca, M.G. Geers, J.P. Hoefnagels, Ferrite slip system activation investigated by uniaxial micro-tensile tests and simulations, Acta Mater. 146 (2018) 314–327.

[66] L. Kar'kina, I. Kar'kin, A. Kuznetsov, Atomistic simulation of stacking faults in (001),(010), and (100) planes of cementite, Phys. Met. Met. 115 (2014) 85–97.

[67] L. Karkina, I. Karkin, I. Kabanova, A. Kuznetsov, Crystallographic analysis of slip transfer mechanisms across the ferrite/cementite interface in carbon steels with fine lamellar structure, J. Appl. Crystallogr. 48 (1) (2015) 97–106.

[68] J. Takahashi, M. Kosaka, K. Kawakami, T. Tarui, Change in carbon state by low-temperature aging in heavily drawn pearlitic steel wires, Acta Mater. 60 (1) (2012) 387–395.

[69] Y. Zhao, Y. Tan, X. Ji, Z. Xiang, Y. He, S. Xiang, In situ study of cementite deformation and its fracture mechanism in pearlitic steels, Mater. Sci. Eng.: A 731 (2018) 93–101.

[70] G.A. Nematollahi, B. Grabowski, D. Raabe, J. Neugebauer, Multiscale description of carbon-supersaturated ferrite in severely drawn pearlitic wires, Acta Mater. 111 (2016) 321–334.

[71] S. Azadehranjbar, B. Wei, D. Xie, K. Ming, J. Wang, J.E. Shield, Strength and plasticity of lamellar vs. fibrous eutectic Mg–Al nanocomposites: An in-situ microcompression study, Acta Mater. 206 (2021) 116624.

[72] H. Chen, L. Lang, X. Shang, S.S. Dash, Y. He, G. King, Y. Zou, Anisotropic co-deformation behavior of nanolamellar structures in additively manufactured eutectic high-entropy alloys, Acta Mater. 271 (2024) 119885.

[73] P. Zhang, Y. Zhou, Y. Liu, S. Li, K. Song, J. Cao, B. Wu, X. Li, H. Wu, J. Gu, et al., Strengthening mechanism of ultra-high strength Cu–20Ag alloy wire induced by cumulative strain, Mater. Sci. Eng.: A 855 (2022) 143957.

[74] Y. Huang, C. Su, H. Lu, Y. Wang, Y. Wang, X. Chen, CoFeNi twisted wire+ Al wire arc additive manufacturing of AlCoFeNi eutectic and near-eutectic high-entropy alloys, J. Mater. Res. Technol. (2024).

[75] J.-X. Chen, T. Li, Y. Chen, F.-H. Cao, H.-Y. Wang, L.-H. Dai, Ultra-strong heavy-drawn eutectic high-entropy alloy wire, Acta Mater. 243 (2023) 118515.

[76] T. Teshima, M. Kosaka, K. Ushioda, N. Koga, N. Nakada, Local cementite cracking induced by heterogeneous plastic deformation in lamellar pearlite, Mater. Sci. Eng.: A 679 (2017) 223–229.